ISSN 1392–1207. MECHANIKA. 2020 Volume 26(5): 375–382

Elastic-plastic Fracture Analysis of External Thread of Drive Shaft Shell of a Positive Displacement Motor

Guanghui ZHAO*, Guipeng LIAO**
**School of Mechanical Engineering, Southwest Petroleum University, Chengdu 610500, China, E-mail: zhaogh@swpu.edu.cn*
***Guangxi Liugong Machinery Co., Ltd., Liuzhou 545007, China, E-mail: 459467380@qq.com*

crossref http://dx.doi.org/10.5755/j01.mech.26.5.24671

1. Introduction

Positive displacement motor (PDM) is a new type of downhole motor that drives drill bit rotating to break rocks. Drilling with PDM has many advantages including high rotation speed, small energy consumption and easy operation. PDM is composed of five assemblies of by-pass valve, anti-drop, power section, universal shaft and drive shaft, as shown in Fig. 1 [1, 2]. Drive shaft assembly is adjacent to the bit, which transmits motor rotary power onto the bit and bears complex impacting loads from the down hole. In accordance with one survey of damaged PDMs in drilling fields, fracture of external joint of drive shaft shell (DSS) is one of the main failure modes of PDMs. This is because that the body of the DSS is more rigid than the threaded joint, and stress concentration always happens to the thread. Under the action of an alternating bending moment caused by lateral force of the bit, the thread root is more likely to crack, and even fracture as a result of crack growth.

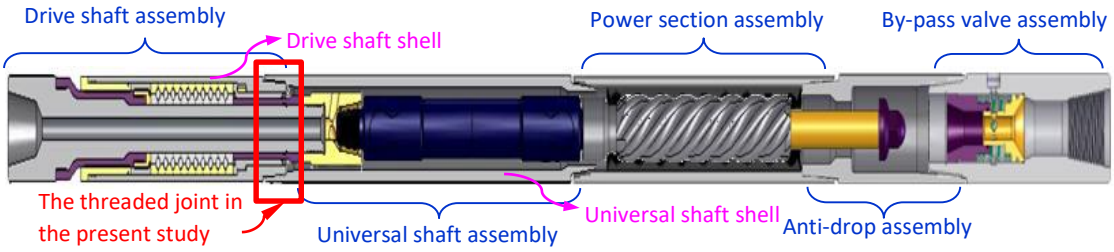

Fig. 1 Composition of a PDM

At present, the failure mechanism of threads is mainly studied by strength or fatigue analysis [3, 4]. Zhu et al. [5] studied mechanical properties of a threaded joint of drive shaft in a PDM under the loading condition of both drilling pressure and torque. It was found that performances of the drive shaft with a straight thread were superior to the one with a taper thread, and the fatigue life of a double-shouldered thread was much longer than that of a single-shouldered one. Liu et al. [6] simulated stress field of a threaded joint of universal shaft shell when passing through the bending section of well. Results indicated that alternating bending load was the main cause of crack initiation and growth. Luo & Wu [7] calculated the stress concentration factor (SCF) of a threaded joint of drill pipe under the action of both tensile and bending load. They found the maximum stress concentration occurred at the root of the first tooth next to the external thread shoulder. It was also the location of crack nucleation. Di et al. [8] paid much attention to effects of bending moment on mechanical behaviours of threaded joints of drill pipes. Results showed that the bending moment direction had an effect on the ultimate working torque of the joint. Shahani & Sharifi [9] carried out a stress analysis for a threaded joint of drill pipe under axial loading with and without pre-load. When pre-load existed, the SCF decreased as the applied load increased, and the fatigue behaviour of the joint was improved.

Based on strength and fatigue analyses, scholars also improve threads in both structure and technology. Zhang et al. [10] proposed a thread with variable-pitch to boost bearing capacities of both tooth bodies and the whole threaded joint. Zhu et al. [11] designed a bevelled shoulder thread with higher strength, larger rigidity and stronger seal performance under the bending moment. Aiming at shearing failure of drill-pipe joints while drilling extended reach wells, Zhu & Zhang [12] proposed an ultra-high torque double-shoulder joint. This joint achieved longer serving life due to feathers including longer primary and secondary shoulders, smaller thread taper and larger fillet radius of bottom tooth. Unlike improving the thread structure, Algimantas et al. [13] presented a new procedural type method, named as duplex positioning method, to increase the operating lifetime of the threaded joint under eccentric loading.

These analyses all aimed at threads without defect, whereas failure of the threaded joint is mostly due to crack propagation. In the study of thread cracking, Liu et al. [14] and Yu et al. [15] carried out failure analyses for the box of the S135 tool joint from five aspects, including materials, crack characteristics, thread tolerances, environmental conditions and service situations. They attributed the micro-crack initiation to both frictions among threads and the corrosion from sulfonated mud. Wang et al. [16] reviewed 21 cases of the longitudinal fractures in tool joint box of drill pipe by means of scanning electron microscopy and energy dispersive X-ray spectrometer. It revealed that crack initiation was caused by tong tooth bite marks, friction damage

and frictional heat check cracking. These researches identified failure causes of threads qualitatively in the way of stress and corrosion. Quantitative relations between the crack growth and outside circumstances were not discussed yet. It is necessary for discovering the failure mechanism of threads that crack evolution is analysed under working conditions.

Surface cracks in a thread usually have irregular shapes. It was suggested that initial surface defects with any shapes would develop into a semi-ellipse shape after several axial loading cycles [17,18]. Elastic fracture properties of both cylinder and tube with a semi-elliptical surface crack have been studied sufficiently [19-21]. But for the thread, which has a helix angle and the region near the crack is usually in an elastic-plastic state under working conditions, the fracture research is few [22, 23].

In this paper, elastic-plastic fracture behaviour of an external thread of DSS, with a circumferential semi-elliptic crack lying at the outer surface of the thread root, is investigated. Firstly, a three-dimensional (3D) FE model of an engaging thread is developed under commercial FE analysis software ANSYS Workbench. Then, interaction between two cracks is discussed. Finally, variation of *J*-integral with crack evolution is formulated.

2. Mechanical model

According to Saint-Venant's Principle, a mechanical model of an engaging thread is established by cutting the DSS and universal shaft shell, as shown in Fig. 2a. Geometric parameters of the threaded joint are shown in Table 1. A semi-elliptical crack is located on the outer surface of the external thread, and the crack surface is in the osculating plane of the root helical line. Fig. 2b shows crack surface, in which the shape of the crack is described by aspect ratio *a/c* and depth ratio *a/t*. *a* and *c* are major and minor axis of the semi-ellipse, and *t* is thickness of the cross section where the crack is located. The deepest point of the crack front is denoted as point *A*, and the boundary point is *B*. An arbitrary point on the crack front is described as S/S_0, in which *S* is the arc length between this point and point *A*, and S_0 is a half arc length of the crack front. Thus $S/S_0 = 0$ is point *A* and $S/S_0 = 1$ is point *B*. Because that stress singularity is different between boundary points and other points, predicted fracture parameters at boundary points are not accurate. Here *J*-integral of the boundary point is taken at point *B*′ that corresponds to $S/S_0 = 0.95$ [19, 24].

Both the DSS and the universal shaft shell are all made of 42CrMo, with elastic modulus E = 212 GPa and Poisson ratio ν = 0.28. The true stress-strain relationship is illustrated in Fig. 3 [25].

The upper end of the internal joint is fixed, and the lower end of the external joint is loaded by a make-up torque *T* and bending moment *M*. Here *T* is set as 39 kN·m according to design parameters of the PDM. The direction of *M* is parallel to the local crack front at point *A*. Considering dynamic effect, the bending moment that comes from lateral collision between bit and borehole wall is chosen as *M* = 8 kN·m. Contact pairs are defined at engaging surface between external and internal thread, and also at shoulder of the external thread, and the friction coefficient μ_n for all the contacted surfaces is all set as 0.1. Contact problem of the engaging thread with 3D crack is highly nonlinear, and it is difficult to converge in simulating elastic-plastic fracture properties under torque. Here make-up torque *T* is converted to pre-load *F* based on the equilibrium condition, and relationship between *T* and *F* is written as

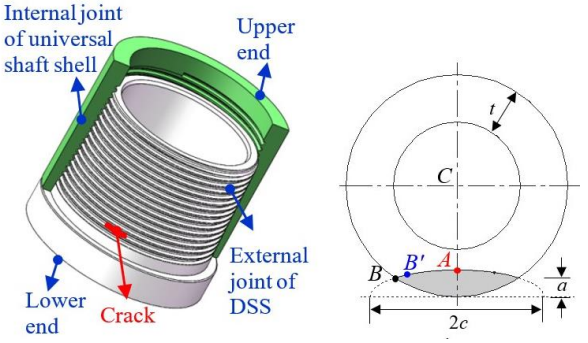

a b

Fig. 2 Sketch of the joint of the DSS: a – model of an engaging thread; b – the cracked cross-section

Table 1

Geometric parameters of the threaded joint

Parameter	Value	Parameter	Value
thread pitch, *P*	6.35 mm	pitch diameter of reference plane	152.31 mm
taper	1:12	external thread length	110 mm
average pitch diameter, d_m	148.90 mm	contact length of internal thread	120 mm
major diameter of big-end of external thread	156.23 mm	internal thread length	130 mm
major diameter of small-end of external thread	147.06 mm	minor diameter of shoulder face, d_1	157.70 mm
outer diameter of lower end, D_L	175 mm	major diameter of shoulder face, d_2	175 mm
inside diameter of lower end, d_L	125 mm	distance of reference plane	15.88 mm

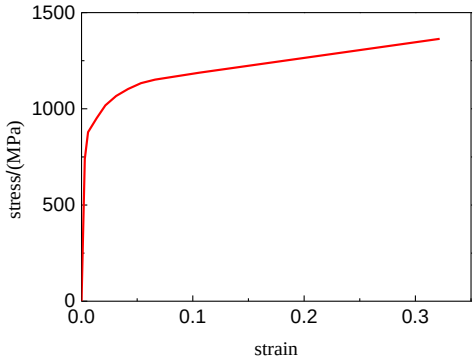

Fig. 3 True stress-strain curve of 42CrMo [25]

$$T = \frac{Fd_m}{2} tan(\alpha + \beta) + \frac{2}{3} \cdot \frac{d_2^3 - d_1^3}{d_2^2 - d_1^2} \mu_n F, \quad (1)$$

where: β is equivalent friction angle of the threaded joint: $\beta = tan^{-1}(\mu_n / cos60^\circ)$; α is average helix angle: $\alpha = arctan[P/(\pi d_m)]$.

Corresponding to T = 39 kN·m, pre-load is obtained as F = 1200 kN that is a tensile distributed force applied on the lower end of the model uniformly.

By means of strength analysis of an un-cracked threaded joint loaded by both make-up torque and bending

moment, it is found that the maximal equivalent stress appears at the first root of the external thread next to the shoulder. It matches up with the damage location of the broken DSS in oil drilling field. In the following sections, elastic-plastic fracture properties of the external thread with a semi-elliptical surface crack at the first root would be simulated.

3. FE model

Considering contact nonlinearity of the threaded joint and the elastic-plastic constitutive relation of the material, a 3D numerical model of the engaged thread, with a surface crack at the first root of the external thread, is developed based on the FE theory. To ensure reliability of the FE model, validation studies are also conducted.

3.1. FE theory of 3D fracture behaviour of the engaging thread

The elastic-plastic fracture analysis of the engaging thread is coupled by both contact nonlinearity and material nonlinearity. Incrementally loading and iteration method need to be used to get stress distribution, through which 3D *J*-integral could be obtained. On the contact surfaces, deformation compatibility condition must be met in the normal direction, and friction condition must be satisfied in the tangential direction. The contact state of the threaded joint could be classified into 3 kinds, such as without contact, bonding contact and sliding contact. On the contact area, friction satisfies Coulomb's law.

Considering the contact conditions of the threaded joint and elastic-plastic constitutive equation of the material, the FE equation could be developed in the global coordinate system by discretizing virtual-work equation of the thread [26]:

$$\left[\boldsymbol{K}\left(\boldsymbol{u}\right)\right]\boldsymbol{u} = \boldsymbol{P} + \boldsymbol{R}\left(\boldsymbol{u}\right), \tag{2}$$

in which, $\boldsymbol{K}(\boldsymbol{u})$ is the global stiffness matrix, which is a function of nodal displacement vector $\boldsymbol{u}$. $\boldsymbol{P}$ is the external force vector acting on the thread. $\boldsymbol{R}(\boldsymbol{u})$ is contact force vector that is a function of relative displacement of contacted point pair. Here two iteration loops exist: one is contact-state iteration and the other one is plastically modifying iteration. During the process of plastically modifying iteration, contact force is obtained by means of the embedded contact-state iteration because that the contact force is influenced by displacement $\boldsymbol{u}$. Eq. (2) could be solved by means of the Newton-Raphson scheme as:

$$\Delta\boldsymbol{u}^{(n)} = -\left[\boldsymbol{K}_T\left(\boldsymbol{u}^{(0)}\right)\right]^{-1}\boldsymbol{\psi}\left(\boldsymbol{u}^{(n)}\right), \tag{3}$$

$$\boldsymbol{\psi}\left(\boldsymbol{u}^{(n)}\right) = \int_V \boldsymbol{B}^T\boldsymbol{\sigma}^{(n)}\mathrm{d}V - \boldsymbol{P} - \boldsymbol{R}\left(\boldsymbol{u}^{(n)}\right) - \Delta\boldsymbol{R}\left(\Delta\boldsymbol{u}^{(n)}\right), \tag{4}$$

$$\boldsymbol{u}^{(n+1)} = \boldsymbol{u}^{(n)} + \Delta\boldsymbol{u}^{(n)}, \tag{5}$$

where: (n) is the iteration step; $[\boldsymbol{K}_T(\boldsymbol{u}^{(0)})]$ is the initial tangent stiffness matrix; $\boldsymbol{\psi}(\boldsymbol{u}^{(n)})$ is the unbalanced force vector; $\sigma^{(n)}$ is the stress vector; $\boldsymbol{B}$ is the strain matrix. $\Delta\boldsymbol{R}$ $(\Delta\boldsymbol{u}^{(n)})$ is the contact force increment, which is obtained during the contact iteration. Finally, convergence criterion of the unbalanced force is examined to judge convergence of the results.

Based on the predicted displacement field, the stress and strain of the thread could be derived through geometric equations and physical equations. Then the *J*-integral could be defined along the crack front:

$$J\left(S\right) = lim_{\Gamma\to 0}\int_{\Gamma}\boldsymbol{n}\cdot\boldsymbol{H}\cdot\boldsymbol{q}\ \mathrm{d}\Gamma, \quad \boldsymbol{H} = W\boldsymbol{I} - \boldsymbol{\sigma}\cdot\frac{\partial\boldsymbol{u}}{\partial x}, \tag{6}$$

where: Γ is a contour in the x_1-x_2 plane that is perpendicular to the crack front at point S (shown in Fig. 4); $\boldsymbol{n}$ and $\boldsymbol{q}$ are all unit vectors in the outward normal direction of Γ and in the crack extension direction, respectively; W is the strain energy density and $\boldsymbol{I}$ is a unit tensor; $\boldsymbol{\sigma}$ is stress tensor and $\boldsymbol{u}$ is displacement tensor.

Based on the equivalent domain integral method proposed by Shih et al. [27], the 3D *J*-integral could be calculated within a small tube surrounding the crack front near point *S*.

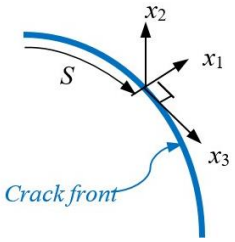

Fig. 4 Local orthogonal Cartesian coordinates at point *S* on the crack front

In the following text, a numerical model of the engaging thread is developed based on the FE method, and the 3D *J*-integral is calculated to show the elastic-plastic fracture behavior of the external joint of DSS.

3.2. FE model and verification

Taking the crack depth ratio of a/t = 0.1 and the aspect ratio of a/c = 0.4 as an example, an FE model containing a cracked external thread of the DSS and an engaging internal thread of the universal shaft shell is established. The mesh model is shown in Fig. 5. In order to improve accuracy, a tubular region around the crack front is refined, and denoted as *refined region*, whose cross-section radius is 0.3 mm. The *refined region* is divided into 8 parts and 16 parts in the radial and circumferential directions, respectively, and 40 parts along the crack front. In the *refined region*, both hexahedron and wedge elements of Solid186 are employed and the element number is n = 7305. The rest of the model is discretized by tetrahedral elements of Solid187, and the areas near the contact surface are also refined to ensure the accuracy of contact analysis. Totally, there are 954811 nodes and 566169 elements in the whole FE model. In the first loading step a pre-load is applied linearly, and a bending moment is exerted in the second loading step while the pre-load remains unchanged.

To ensure the correctness of the FE analysis, both convergence of space step and conservation of *J*-integral are studied, and the predicted results of a cracked bolt are compared with that of a published literature.

Convergence study of space step is conducted by altering mesh size in the *refined region*. The element number of the *refined region* is chosen as n = 384, 2168, 4392 and 7305, respectively, and the predicted J-integrals of the deepest point A of the crack front are given in Table 2. Taking the J-integral corresponding to n = 7305 as a reference, relative errors corresponding to different mesh densities are also listed in Table 2.

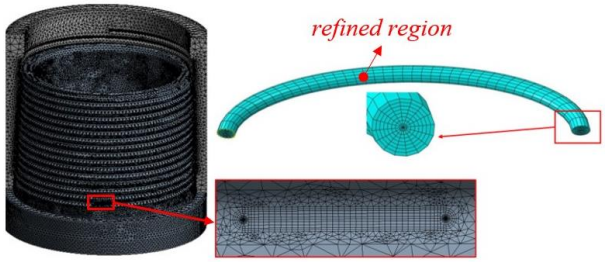

Fig. 5 FE discretization of the cracked joint

Table 2

J-integral and relative error for point A corresponding to different mesh densities

Element number n of the *refined region*	384	2168	4392	7305
J-integral, MPa·mm	3.352	3.425	3.450	3.480
Relative error, %	3.6	1.5	0.8	/

It is concluded that the calculated results are converged with mesh refining. Considering the complexity of thread contact analysis, the FE mesh with n = 7305 as shown in Fig. 5 is employed here.

To verify the conservation of the predicted J-integral, 8 contours are defined in the normal plane at each point of the crack front. Variations of these 8 contour integrals along the crack front are presented in Fig. 6. Except for the first 2 contour integrals, the other 6 integrals are all close to each other. Here the average value of the 6th, 7th and 8th contour integrals is defined as J-integral, and the maximal relative error among these three values is only 0.06%. It indicates that the simulated J-integral is conservative and the numerical method is valid.

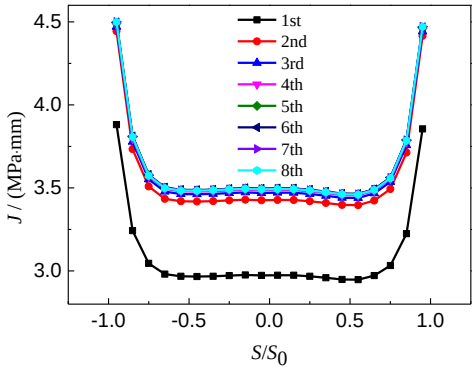

Fig. 6 Contour integrals along the crack front

Due to the lack of experimental results on the elastic-plastic fracture properties of cracked threads, the present FE model is verified by comparing the elastically predicted results of a cracked bolt with that of Ref. [22]. According to Ref. [22], an FE model is developed for an engaging bolt with a semi-elliptical surface crack at the root of the external thread. The crack depth ratio a/d is 0.1 and the aspect ratio a/c is 0.2, where d is minor diameter of the bolt. The threaded bolt is discretized according to the above meshing method, as shown in Fig. 7. As Ref. [22], a dimensionless stress intensity factor (SIF), denoted as K_0, is defined as $K_0 = \sqrt{K_I^2 + K_{II}^2 + K_{III}^2}/(1-\nu)/\sigma\sqrt{\pi a}$, in which K_{I}, K_{II} and K_{III} are SIFs of mode I, II and III respectively, and σ is the nominal tensile stress. The calculated K_0 distribution along the crack front is compared with the results of Ref. [22], and the maximum relative error is only 6.6%, which indicates that the present FE method is reliable. So the FE model shown in Fig. 5 would be used to study the elastic-plastic fracture performance of the threaded joint of the DSS.

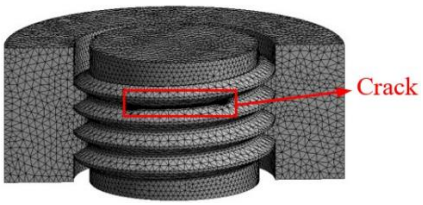

Fig. 7 FE discretization of the cracked bolt

4. Fracture properties of the threaded joint

The thread has a helix angle and the region near the crack is usually in an elastic-plastic state under working conditions. Due to the complexity of the problem, elastic fracture analysis is often conducted without considering the helix angle, while the error generated by this simplified model is rarely mentioned. Based on the FE model of Sec. 3.2, the fracture performance of cracked external thread of the DSS is simulated under the combined action of pre-load and bending moment. Effects of both plastic deformation and the helix angle on the fracture prediction are evaluated, and influence of a vice crack on the main crack is also discussed.

4.1. Effect of plastic deformation

Taking cracks of a/c = 0.4 and a/t = 0.1, 0.3, 0.5 and 0.7 as examples, J-integrals are calculated based on the elastic constitutive model and the elastic-plastic constitutive model, respectively. The elastic result J_e and the elastic-plastic result J are obtained along the crack front, as shown in Fig. 8, where dotted lines correspond to the elastic result J_e and solid lines to the elastic-plastic result J. For the crack

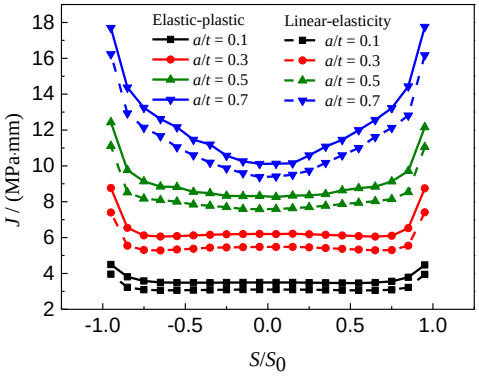

Fig. 8 Predicted J-integrals with elastic and elastic-plastic contitutive models, respectively

with a certain *a/t*, elastic-plastic results *J* are all larger than corresponding elastic results J_e. Therefore, evaluation on fracture behavior is unsafe if the plastic deformation is not taken into account. Here the plastic part of *J*-integral is defined as $J_P = J - J_e$, and J_P/J is used to describe effects of plastic deformation on fracture properties quantitatively. For the cracks of *a/t* = 0.1, 0.3, 0.5 and 0.7, J_P/J for the deepest point *A* of the crack front is 11.2%, 11.8%, 8.4% and 7%, respectively. Due to the complexity of the thread structure and the crack location, variation of J_P /*J* with *a/t* is not monotonic.

4.2. Effect of the helix angle condition

The joint model *without* helix angle condition is established as shown in Fig. 9, whose FE model is developed with the same parameters as the model with helix angle condition, including the crack location, meshing method, loading steps and boundary conditions. Attention is needed that the crack surface is perpendicular to the pre-load for the model *without* helix angle condition, and the crack is mode *I*. But for the model with helix angle condition, the crack surface is not perpendicular to the pre-load and the crack is mixed-mode. For semi-elliptic surface cracks of *a/c* = 1 and *a/t* = 0.1, 0.3, 0.5 and 0.7 respectively, effects of helix angle on fracture behaviors of the cracked thread are studied using these two models. The distribution of *J*-integrals along the crack front is shown in Fig. 10, where solid lines are results with helix angle condition, and dotted lines are results *without* helix angle consideration. It can be seen that the results considering of the helix angle are all greater than that *without* helix angle. For the crack of *a/t* = 0.1, 0.3, 0.5 and 0.7, compared with the predicted results considering of helix angle, the relative errors of the *J*-integral *without* helix angle consideration are 9.7%, 9.5%, 10.2% and 12.8%, respectively, for the deepest point *A* of the crack front. Therefore, the fracture evaluation is also dangerous if the helix angle is not considered.

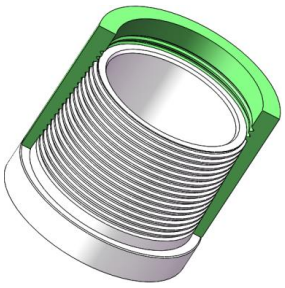

Fig. 9 Model of the engaging thread *without* helix angle

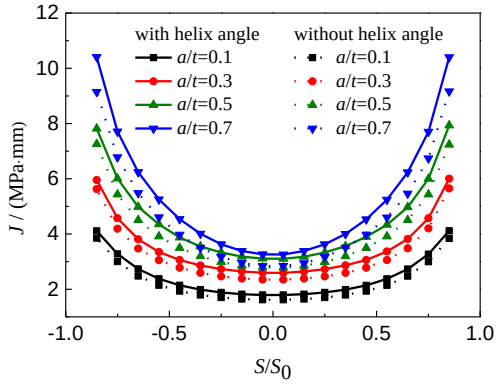

Fig. 10 Effect of helix angle condition on *J*-integral

4.3. Interaction of two cracks

Due to the complexity of both thread structure and stress state, multiple cracks may coexist in the area of stress concentration. It may influence fracture behaviors of the thread that multiple cracks interact each other. Here a main crack of *a/c* = 0.4 and *a/t* = 0.3 is at the first thread root of the external joint, and a vice crack is located at the root of the second thread and parallel to the main crack, as illustrated in Fig. 11. Effects of the vice crack on fracture behaviors of the main crack are studied.

Firstly, the effect of the vice crack with different aspect ratio on fracture behaviors of the main crack is studied. For the vice crack, the depth ratio *a/t* is kept as 0.4, and *a/c* is set as 0.2, 0.4, 0.6 and 0.8, respectively. The distribution of *J*-integral along the crack front of the main crack is presented in Fig. 12, in which *J*-integral *without* vice crack is also given for reference. It shows that appearance of the vice crack reduces the *J*-integral of the main crack significantly. This tendency is consistent with the crack shielding effect described by O′ Hara et al. [28]. With the decrease of *a/c* of the vice crack, the *J*-integral of the main crack decreases correspondingly. It is because that a smaller *a/c* leads to a larger crack surface area, which exerts stronger shielding effect on the main crack.

Secondly, the effect of the vice crack with different depth ratio on the main crack is also analyzed. The aspect ratio *a/c* of the vice crack is set as 0.4, and the depth ratio *a/t* is chosen as 0.1, 0.3, 0.5 and 0.7, respectively. The *J*-integral of the main crack, influenced by the vice crack, is presented in Fig. 13. It can be seen that the *J*-integral of the main crack decreases gradually as the depth ratio *a/t* of the vice crack increases. This also could be explained by crack shielding effect. Larger *a/t* of the vice crack means larger crack surface, which has larger shielding effect on the main crack.

The vice crack located at the root of the adjacent thread has shielding effect on the main crack. The larger the vice crack surface is, the larger shielding effect is. There-

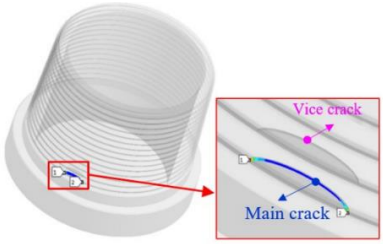

Fig. 11 External thread with two cracks

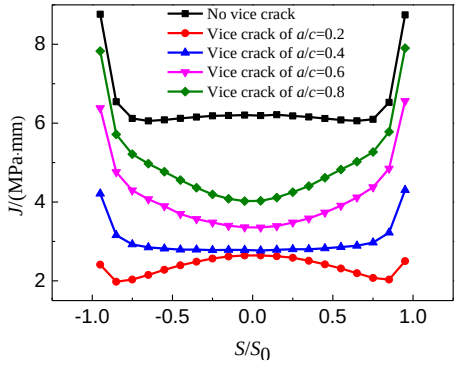

Fig. 12 Variation of *J*-integral along the main crack front under different *a/c* of the vice crack

fore, the presence of the vice crack does not reduce the fracture strength of the main crack. As a result, fracture behaviors will be discussed under the condition that only one crack exists at the first root of the external thread.

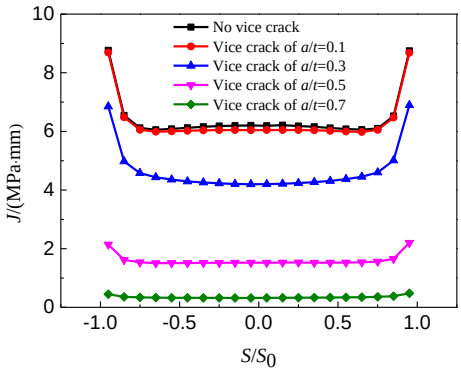

Fig. 13 Variation of *J*-integral along the main crack under ifferent *a/t* of the vice crack

5. Variation of *J*-integral with crack propagation

Similar to Paris' law that is used to describe high-cycle fatigue life, the crack growth rate *da/dN* is related to the amplitude of *J*-integral, ΔJ, for low-cycle fatigue problem, and described by:

$$da/dN = C \cdot (\Delta J)^m , \tag{7}$$

in which *C* and *m* are material constants, $\Delta J = J_{max} - J_{min}$. For the threaded joint of the DSS, the pre-load *F* always exists in the course of drilling operation, while lateral impact between the bit and bottom hole is intermittent. This lateral impact leads to alternating bending moment *M* that is responsible for the thread fatigue. Therefore, J_{min} corresponds to the loading condition of *F*, and J_{max} is the *J*-integral under the action of both *F* and *M*. In order to make the results more general, the dimensionless *J*-integral, denoted as J_0, is defined by:

$$J_0 = J\bar{E} / (\pi a \sigma^2), \tag{8}$$

where: $\bar{E} = E/(1-\nu^2)$ for plane strain and $\bar{E} = E$ for plane stress. $\sigma = F / A_m$ corresponding to loading conditions of only *F*, and $\sigma = F / A_m + M / W$ corresponding to loading conditions of both *F* and *M*. A_m and *W* are area and elastic section modulus, respectively, of the lower end section of the external joint. It can be obtained as A_m = 11,781 mm^2 and *W* = 389,193 mm^3 according to dimensions shown in Table 1. Therefore, σ is calculated as 102 MPa under the loading of *F*, and σ is 122 MPa under the loading of both *F* and *M*.

Along with crack fatigue growth, *J*-integrals tend to the same value for all points of the crack front. For a certain crack depth, a critical aspect ratio $(a/c)_c$, which describes the shape of fatigue crack, is determined when the *J*-integral of point *A* ($S/S_0 = 0$) equals to that of point *B*′ ($S/S_0 = 0.95$) (Fig. 2, b), and this *J*-integral is defined as characteristic *J*-integral J_c. So, variation of J_c with crack propagation could be used to predict fatigue life of the cracked joint.

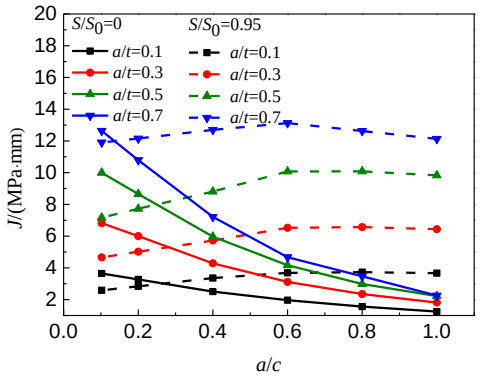

a

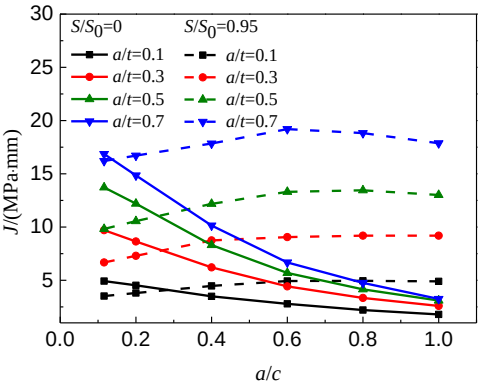

b

Fig. 14 Determination of $(a/c)_c$ and J_c: a – loaded by pre-load only; b – loaded by both pre-load and bending moment

For the cracks of *a/t* = 0.1, 0.3, 0.5 and 0.7, variations of *J*-integrals along with *a/c* for both point *A* and point *B*′ are calculated and given in Fig. 14, in which Fig. 14, a corresponds to the loading condition of pre-load and Fig. 14, b is the outcome of both pre-load and bending moment. Solid and dotted lines correspond to point *A* and point *B*′, respectively. The point of interaction of the solid and dotted curves gives $(a/c)_c$ and J_c for a certain crack depth as shown in Fig. 14, a, in which *a/t* = 0.3 is taken as an example. The predicted $(a/c)_c$ and J_c for different crack depth are presented in Table 3. It is found that J_c increases with crack growth under these two loading conditions.

Using Eq. (8) dimensionless characteristic *J*-integral, denoted as J_{0c}, could be derived. In the loading case of pre-load alone, the variation of J_{0c} with *a/t* is fitted by a polynomial as shown in Eq. (9) and Fig. 15, a:

$$J_{0c} = 106.02(a/t)^4 - 262.74(a/t)^3 + \\ +245.79(a/t)^2 - 100.85(a/t) + 23.577, \tag{9}$$

And in the loading case of both pre-load and bending moment, relationship between J_{0c} and a/t is shown in Eq. (10) and Fig. 15, b:

$$J_{0c} = 46.826(a/t)^4 - 141.5(a/t)^3 + 155.43(a/t)^2 - 73.213(a/t) + 20.615. \tag{10}$$

Table 3

$(a/c)_c$ and J_c for different a/t

	a/t	0.1	0.2	0.3	0.4	0.5	0.6	0.7	0.8
loaded by pre-load only	$(a/c)_c$	0.268	0.275	0.28	0.271	0.249	0.231	0.134	0.104
	J_c, MPa·mm	3.01	4.29	5.30	6.59	7.99	9.56	12.02	13.86
loaded by both pre-load and bending moment	$(a/c)_c$	0.285	0.263	0.269	0.267	0.26	0.212	0.139	0.116
	J_c, MPa·mm	4.08	6.02	7.80	9.32	11.03	13.29	16.33	18.13

Explicit expression of *J*-integral along with crack growing is essential in predicting fatigue life of the structure based on the method of fracture mechanics. By means of Eq. (1) and Eqs. (7)- (10), the fatigue life of the threaded joint of the DSS could be estimated if the parameters, including pre-load, bending moment, *C* and *m*, the initial and critical crack depth, are given.

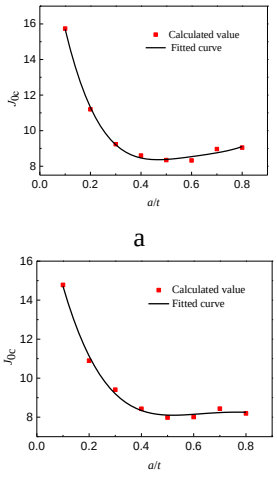

a

b

Fig. 15 Variation of J_{0c} along with crack growth: a – exerted by pre-load only; b – exerted by both pre-load and bending moment

6. Conclusions

Based on the drilling load of the PDM, a 3D FE model of an engaging thread of the DSS, with a semi-elliptical surface crack on the root of the external joint, is developed. Elastic-plastic fracture properties of the joint are analysed under the loading condition of both make-up pre-load and bending moment. The main conclusions are drawn as follows:

1. The calculated *J*-integral based on the elastic-plastic constitutive relation is larger than the elastic result. The fracture evaluation is unsafe if the plastic deformation of the material is neglected in the model.

2. The helix angle has influence on the predicted *J*-integral, and the numerical results are also dangerous if the helix angle is not taken into account.

3. The vice crack, located at the root of the adjacent thread, has shielding effect on the main crack. So, presence of vice crack does not reduce the fracture strength of the main crack.

4. Variations of dimensionless characteristic *J*-integrals with crack growth are presented under the two kinds of loading conditions, one is action of pre-load only and the other one is combined action of both pre-load and the bending moment. These explicit expressions could be used to predict the fatigue life of the threaded joint of the DSS in the course of operation.

Acknowledgments

This project was supported by the Open Fund of Key Laboratory of Oil & Gas Equipment, Ministry of Education (SWPU).

References

1. **Zhang, J.; Han, C.J.; Liang, Z.** 2016. Physics of failure analysis of power section assembly for positive displacement motor, Journal of Loss Prevention in the Process Industries 44: 414-423. http://dx.doi.org/10.1016/j.jlp.2016.10.020.
2. **Nguyen, T. C.; Al-Safran, E.; Nguyen, V.** 2018. Theoretical modeling of positive displacement motors performance, Journal of Petroleum Science and Engineering 166: 188-197. http://dx.doi.org/10.1016/j.petrol.2018.03.049.
3. **Wentzel, H.; Huang, H.Y.** 2015. Experimental characterization of the bending fatigue strength of threaded fasteners, International Journal of Fatigue 72: 102-108. http://dx.doi.org/10.1016/j.ijfatigue.2014.11.005.
4. **Matsunari, T.; Oda, K.; Tsutsumi, N.; Yakushiji, T.; Noda, N. A.; Sano, Y.** 2018. Experimental study on the effect of shape of bolt and nut on fatigue strength for bolted joint. IOP Conference Series: Materials Science and Engineering 372: 012016. http://dx.doi.org/10.1088/1757-899X/372/1/012016.
5. **Zhu, X. H.; Lin, D.; Li, J. N.** 2016. Failure analysis and structure optimization of the connecting thread of driving shaft in positive displacement motor, Advances in Mechanical Engineering 8(6): 1-11. http://dx.doi.org/10.1177/1687814016652313.
6. **Liu, Y.; Lian, Z. H.; Qian, L.Q.; Xia, C. Y.; Zhang, J.; Tu, Y. L.** 2018. Fracture failure analysis and research on special taper thread of cardan shaft Shell of PDM, Engineering Failure Analysis 86: 44-55. https://doi.org/10.1016/j.engfailanal.2017.12.007.
7. **Luo, S.; Wu, S.** 2013. Effect of stress distribution on the tool joint failure of internal and external upset drill pipes, Materials & Design 52(24): 308-314. http://dx.doi.org/10.1016/j.matdes.2013.05.07.
8. **Di, Q.F.; Song, H.T.; Chen, F.; Zhang ,H.; Wang, W.C.; Li, N.** 2016. The effect of bending moment direction on tool joints: working load limits under complex loads, Journal of Natural Gas Science and Engineering 35: 532-540. http://dx.doi.org/10.1016/j.jngse.2016.09.007.
9. **Shahani, A. R.; Sharifi, S. M. H.** 2009. Contact stress analysis and calculation of stress concentration factors at the tool joint of a drill pipe, Materials & Design 30(9): 3615-3621. http://dx.doi.org/10.1016/j.matdes.2009.02.022.
10. **Zhang, S. L.; Li, D. R.; Zhang, J.; Lu, B.** 2013. Experimental research on connection performance of variable-

pitch threaded casing, Advanced Materials Research 805-806: 1805-1811. http://dx.doi.org/10.4028/www.scientific.net/AMR.805-806.1805.
11. **Zhu, X. H.; Dong, L. L.; Tong, H.** 2013. Failure analysis and solution studies on drill pipe thread gluing at the exit side of horizontal directional drilling, Engineering Failure Analysis 33: 251-264. http://dx.doi.org/10.1016/j.engfailanal.2013.05.017.
12. **Zhu, X. H.; Zhang, Z.** 2017. Design of an ultra-high torque double shoulder drill-pipe tool joint for extended reach wells, Natural Gas Industry B 4: 374-381. https://doi.org/10.1016/j.ngib.2017.10.002.
13. **Krenevicius, A.; Kacianauskas, R.; Selivonec, J., Stupak, S.** 2017. Duplex positioning method for increasing the fatigue life of threaded connections under eccentric loading, Journal of Mechanical Science and Technology 31 (2): 733-752. http://dx.doi.org/10.1007/s12206-017-0125-1.
14. **Liu, W. Y.; Liu, Y.; Chen, W. J.; Shi, T. H.; Singh, A.; Lu, Q.** 2015. Longitudinal crack failure analysis of box of S135 tool joint in ultra-deep well, Engineering Failure Analysis 48: 283-296. http://dx.doi.org/10.1016/j.engfailanal.2014.11.022.
15. **Yu, S. J.; Yuan, P. B.; Deng, K. H.; Liu, W. Y.; Lin, Y. H.; Zhang, J.** 2018. Experimental and numerical study on the longitudinal-crack failure of double-shoulder tool joint, Engineering Failure Analysis 91: 1-11. https://doi.org/10.1016/j.engfailanal.2018.04.017.
16. **Wang, X. H.; Li, F. P.; Liu, Y. G.; Feng, Y. R.; Zhu, L. J.** 2017. A comprehensive analysis on the longitudinal fracture in the tool joints of drill pipes, Engineering Failure Analysis 79: 1-7. http://dx.doi.org/10.1016/j.engfailanal.2017.03.019.
17. **Lin, X. B.; Smith, R. A.** 1997. Shape growth simulation of surface cracks in tension fatigued round bars, International Journal of Fatigue 19(6): 461-469.
18. **Zhao, G. H.; Li, J.; Zhang, Y. X.; Zhong, J. J.; Liang, Z.; Xiao, S. H.** 2019. A study on ductile fracture of coiled tubing based on cohesive zone model, Engineering Fracture Mechanics 209: 260-273. https://doi.org/10.1016/j.engfracmech.2019.01.027.
19. **Zhao, G. H.; Li, J.; Zhang, Y. X.; Liang, Z.** 2018. An inverse analysis-based optimal selection of cohesive zone model for metallic materials, International Journal of Applied Mechanics 10(2): 18500151 (19 pages). https://doi.org/10.1142/S1758825118500151.
20. **Li, Y. S.;Hasegawa, K.; Katsumata, G.; Osakabe, K.; Okada, H.** 2015. Development of stress intensity factors for surface cracks with large aspect ratio in plates, Journal of Pressure Vessel Technology 137(5): 051207. http://dx.doi.org/10.1115/1.4030026.
21. **Zhang, Y. Z.; Shi, Z. J.; Tian, D. Z.; Gong, C.; Peng, L. M.** 2018. Finite element analysis of dynamic fracture behaviour of drill pipe under various impact loads, Mechanika 24(4): 404-411. http://dx.doi.org/10.13225/j.cnki.jccs.2010.07.004.
22. **Kumar, S. S.; Prakash, R. V.** 2013. Effect of helix angle on the stress intensity factor of a cracked threaded bolt, Journal of Pressure Vessel Technology 135(2): 21202. https://doi.org/10.1115/1.4007290.
23. **Sundaram, S. K.; Prakash, R. V.** 2015. Effect of loading condition on stress intensity factor for threaded fasteners under helix angle condition, International Mechanical Engineering Congress and Exposition. Houston, ASME: 1-10.
24. **Shahani, A. R.; Habibi, S. E.** 2007. Stress intensity factors in a hollow cylinder containing a circumferential semi-elliptical crack subjected to combined loading, International Journal of Fatigue 29(1): 128-140. http://dx.doi.org/10.1016/j.ijfatigue.2006.01.017.
25. **Zhu, Z. W.; Lu, Y.; Xie, Q. J.; Li, D. Y.; Gao, N.** 2017. Mechanical properties and dynamic constitutive model of 42CrMo steel, Materials & Design 119: 171-179. http://dx.doi.org/10.1016/j.matdes.2017.01.066.
26. **Bathe, K. J.** 1996. Finite element procedures, Prentice Hall, Upper Saddle River, New Jersey 07458.
27. **Shih, C. F.; Moran, B.; Nakamura, T.** 1986. Energy release rate along a three-dimensional crack front in a thermally stressed body, International Journal of Fracture 30(2): 79-102.
28. **O'Hara, P.; Duarte, C.A.; Eason, T.** 2016. A two-scale generalized finite element method for interaction and coalescence of multiple crack surfaces, Engineering Fracture Mechanics 163: 274-302. http://dx.doi.org/10.1016/j.engfracmech.2016.06.009.

G. H. Zhao, G.P. Liao

ELASTIC-PLASTIC FRACTURE ANALYSIS OF EXTERNAL THREAD OF DRIVE SHAFT SHELL OF A POSITIVE DISPLACEMENT MOTOR

S u m m a r y

For a positive displacement motor (PDM), the threaded joint connecting drive shaft shell (DSS) and universal shaft shell that is close to the bit is inclined to fracture. In this paper, elastic-plastic fracture performance of the threaded connection is simulated under both make-up torque and bending moment. Firstly, an FE model, which includes a cracked external thread of the DSS and an engaging internal thread of the universal shaft shell, is established and validated. Secondly, influences of both plastic deformation and the helix angle on fracture properties of the cracked thread are evaluated quantitatively. Meanwhile interactions between two cracks are also discussed. Finally, under the two kinds of loading conditions, i.e. loaded by pre-load only and loaded by both pre-load and bending moment, explicit relationships between characteristic *J*-integrals and the crack depth are obtained for the DSS.

Keywords: positive displacement motor (PDM); threaded joint; surface crack; elastic-plastic fracture; helix angle.

Received November 23, 2019
Accepted October 14, 2020